J Mater Sci: Mater Electron (2021) 32:27801–27814

Structural and electrical transport properties of Ge implanted $CoSb_3$ thin films and their conduction mechanisms

Anha Masarrat[1,2], Anuradha Bhogra[1], Ramcharan Meena[1], M. Sinduja[3], Dilruba Hasina[4], S. Amirthapandian[3], Devarani Devi[1], Tapobrata Som[4], A. Niazi[2,*], and Asokan Kandasami[1,5,*]

[1] *Inter-University Accelerator Centre, Aruna Asaf Ali Marg, New Delhi 110067, India*
[2] *Department of Physics, Jamia Millia Islamia, New Delhi 110025, India*
[3] *Materials Physics Division, Indira Gandhi Centre for Atomic Research, HBNI Kalpakkam, Kalpakkam 603102, India*
[4] *Institute of Physics, Bhubaneswar 751005, India*
[5] *Department of Physics & Centre for Interdisciplinary Research, University of Petroleum and Energy Studies (UPES) Dehradun, Uttarakhand 248007, India*

Received: 19 July 2021
Accepted: 30 September 2021
Published online:
18 October 2021

© The Author(s), under exclusive licence to Springer Science+Business Media, LLC, part of Springer Nature 2021

ABSTRACT

The structural and electrical transport properties of Ge ion-implanted $CoSb_3$ thin films were investigated. These thin films were deposited by pulsed laser deposition on the quartz substrates and 100 keV Ge ions were implanted with the ion fluences ranging from 5×10^{14}, 1×10^{15} to 5×10^{15} ions/cm^2. Scanning electron microscopy shows an enlargement in grains with the increase of ion fluence which is attributed to the contribution from local annealing and the creation of ion-induced defects. The electrical resistivity (ρ) measurements indicate that Ge implantation strongly influences the temperature-dependent resistivity and hence affect the charge carriers. The decrease in mobility and an increase in carrier concentration with the ion fluences lead to a decrease in electrical resistivity. The conduction mechanism study reveals that this system exhibits Mott type variable range hopping characteristics ($\ln \rho \propto 1/T^{1/4}$) in the low-temperature regime for all the samples and follow the small polaron hopping conduction mechanism, $\ln (\rho/T) \propto 1/T$, at high temperature up to 400 K. The room temperature Hall effect measurement and the temperature-dependent Seebeck effect reveal that these films are of *n*-type.

Address correspondence to E-mail: aniazi@jmi.ac.in; asokaniuac@gmail.com

https://doi.org/10.1007/s10854-021-07163-z

1 Introduction

Several concepts are being proposed for a material to be a good thermoelectric (TE) material [1, 2]. One such concept is the phonon glass electron crystal (PGEC) introduced by Slack [3]. The materials that follow the concept of PGEC possess the thermal conductivity as that of glass while having the electrical conductivity as that of metal [4]. One such material is skutterudite in the form MX_3 (where M is metal like Co, Ir and X is metalloid like Sb, As, P) [5, 6]. These materials are one of the potential TE materials that are in continuous research of interest [7]. The skutterudites possess a complex structure, low electronegativity difference between the constituent atoms, high carrier mobility and modest thermopower [8, 9]. $CoSb_3$ have been identified as one of the strong skutterudite candidates for TE applications. It has a cubic structure with the Im-3 space group having a bandgap of 0.5 eV [4]. It consists of eight sub cubes out of which six are occupied with four-membered square planar Sb rings that are arranged parallel to the crystallographic axis. In the unit cell, eight $CoSb_6$ octahedra share the corners of the cubic lattice forming the $(CoSb_6)_8$ cluster. A void or a vacant site is created at the centre of this cluster. These voids act as a home for foreign atoms that could be loosely bound and could rattle inside the cage structure. Some atoms like Ba, Ge, rare earth metals etc. can occupy the voids and rattle inside them. These rattlers scatter a large number of phonon frequencies and substantially lower the lattice thermal conductivity of the material [4, 10–14]. Further, the ternary skutterudites can be formed by doping them by dopants (Fe, Ni, Ge, etc.) at Co or Sb site to achieve high TE efficiency [15–18]. The efficiency of a TE material is defined by the figure of merit, zT, a dimensionless quantity $zT = \frac{S^2T}{\rho\kappa}$, where S is Seebeck coefficient or thermopower, T temperature, ρ resistivity and κ is total thermal conductivity, which is a sum of κ_L (lattice thermal conductivity) and κ_E (electronic thermal conductivity) [19]. The core properties required in material for good zT, as suggested by Slack [3], like large unit cell, high carrier mobility and complex structure are found in these skutterudites. The doping at Co or Sb site or filling the void can modify the electronic structure and electrical properties along with affecting the lattice thermal conductivity [20, 21]. However, in the bulk system, the main complication is the interdependence of electrical conductivity and thermopower (S), as tuning of one quantity influences the other. Hence, it is necessary to find promising TE properties in $CoSb_3$ thin film. Ion implantation is one of the ways to modify the low dimensional systems and simultaneously doping or filling the voids in a controlled manner. In ion implantation, highly energetic ions penetrate the host material depending upon the energy and mass of the ion. This provides several ways to alter the conducting properties by introducing chemical as well as structural changes. Hence, it can facilitate the tuning of the electrical properties by varying the carrier concentration, creating defects and or by producing nanostructures. Bala et al. [22] and Masarrat et al. [23] reported the Ni and Fe ion implantation studies on $CoSb_3$ respectively. Bala et al. [24] in another study used the ion implantation technique for doping Ag in the PbTe thin films and reported 25% enhancement in the Seebeck coefficient. It is important to note that there are limited investigations on ion implantation studies of $CoSb_3$. Hence, it is an open field to study the modification of the physical properties of this compound through the ion beam techniques. Understanding the electrical properties and the conduction mechanisms are important to further correlate with the physical properties including the TE properties. Ge can be accommodated in the voids as well as it can substitute the Sb position in the $CoSb_3$ lattice. Nolas et al. [17] studied the physical properties of Ge filled $CoSb_3$ synthesised by high-pressure technique. These authors employed very high pressure to squeeze Ge atoms inside the voids. Further, they have made a systematic investigation by filling the $IrSb_3$ voids with rare-earth ions (La and Sm) and substituted Ge for Sb for charge compensation and reported that the rattling method is one of the most promising methods for the decrease of thermal conductivity [25]. In another study, Shaheen et al. [26] studied the TE properties of Ge doped Nd filled skutterudite compound. They have synthesised the p-type skutterudite through homemade melt induction followed by spark plasma sintering and reported a high zT of 0.82, which was 30% higher than that of the Ge free sample. The Ge atom in the $CoSb_3$ structure can act as an electron acceptor by substituting at the Sb site and also as an electron donor when it occupies the voids of the $CoSb_3$ structure [17, 27, 28]. This study focuses on the Ge ion implantation in the $CoSb_3$ matrix and its effects on the morphological, structural and electrical properties. The detailed analysis of the conduction mechanisms in the ion-implanted $CoSb_3$ is an imperative tool to tailor the TE properties. This investigation provides an insight

into the conduction mechanisms that govern at different temperature ranges.

2 Experimental details

The $CoSb_3$ thin films were grown on a quartz substrate using the pulsed laser deposition (PLD) system from M/S Excel Instruments, India. The commercial bulk $CoSb_3$ was used as the target. The substrate temperature was maintained at 523 K with a background Ar gas pressure of 1.3 Pa, and a target-to substrate distance of 6 cm. A detailed procedure for deposition of these films using PLD and a description of the effects of deposition parameters like stress, composition, and crystallinity on $CoSb_3$ have been published elsewhere [23]. These films were implanted with 100 keV Ge ions using the Inter-University Accelerator (IUAC) facility, India for Negative Ion Implantation with the ion fluences: 5×10^{14}, 1×10^{15} and 5×10^{15} ions /cm^2. In the ion implantation, the ion beams were scanned over an area of 1 cm $\times$ 1 cm for uniformity. The implantation was carried out at room temperature in the vacuum chamber maintained at 10^{-4} Pa.

In this study, the pristine thin film is referred to as GCS1, and the implanted films with ion fluences 5×10^{14} ions/cm^2, 1×10^{15} ions/cm^2 and 5×10^{15} ions/cm^2 are refereed as GCS2, GCS3 and GCS4 respectively. The thickness of the as-deposited thin film was evaluated using Rutherford backscattering (RBS) and found to be 300 nm. The projected range of the Ge ion beam is 29 nm with a straggling of 17 nm as calculated through stopping and range of ions in matter (SRIM) [29]. Based on this, it is found that the $\sim$ 46 nm thick layer is amorphized. The atomic force microscopy (AFM) was performed to study the surface morphology using the Multi-Mode Scanning Probe Microscopy (Witec Alpha RA 300) operated under tapping mode. A scanning electron microscope (SEM) was used to study the surface morphology using the focussed ion beam field emission scanning electron microscope (FIB-FESEM, Zeiss, crossbeam 340). The FIB-FESEM was operating at an accelerating voltage of 5 kV with a working distance of 3 mm. The images were recorded using the in-lens detector. The structural characterizations were performed by using the grazing incidence X-Ray Diffraction (GIXRD) at 1° of the Philips X'pert PRO (Model PW 3040) diffractometer and the micro-Raman measurements by using Micro Raman spectroscopy (m-RS, Renishaw, UK). The Hall effect measurement was carried out using a 0.57 T magnetic field at room temperature to calculate the carrier concentration and mobility. The temperature-dependent electrical resistivity (ρ) in the range of 80 to 400 K was measured by the four-probe method and the Seebeck coefficient (S) by the bridge method [30] in the temperature range from 300 to 400 K.

3 Results and discussion

3.1 Morphological analysis

The morphology of the samples GCS1, GCS2, GCS3 and GCS4 are displayed in Fig. 1. From the SEM images, it is observed that angular grains and visible grain boundaries are distinct and clear for the pristine sample. Ion implantation causes the morphology changes and the well-defined grains gradually disappear. A similar trend was also observed for Ge doped In-filled Co_4Sb_{12} samples [28], where well-defined grains disappear with the change in Ge content. Similar grain boundaries disappearance and microstructure changes were also observed with Te substitution in $CoSb_3$ [31]. The grain size has been calculated by measuring the size of 50 grains and then averaging it to obtain the average grain size for each sample. For GCS1, the average grain size is found to be 148 nm, which is smaller than that of the sample implanted with 5×10^{14} ions/cm^2. The grain size increases further as the ion fluence increases and reaches 250 nm for GCS3. This increase in grain size may be attributed to the local annealing caused during ion implantation [32]. Ion implantation produces beams of sufficient power density to raise the temperature of the target by 100s of degrees which gets dispersed into the surrounding solid within 10^{-9} s. During this brief period of high atomic mobility, substantial rearrangement of atoms occurs that can lead to grain growth. In this study, one expects that the local heat generated due to the energy loss leads to the grain growth due to ion implantation. The grain growth with ion fluence may also be attributed to the defects created due to ion implantation. Both nuclear energy loss (S_n) and electronic energy loss (S_e) take place during the ion beam process. They may contribute to grain enlargement. The S_n and S_e are calculated using SRIM and found to be 156 eV/Å and 19.69 eV/Å, respectively. Due to high S_n during implantation, extended damages lead to the creation of defects through nuclear collisions. Further, when an

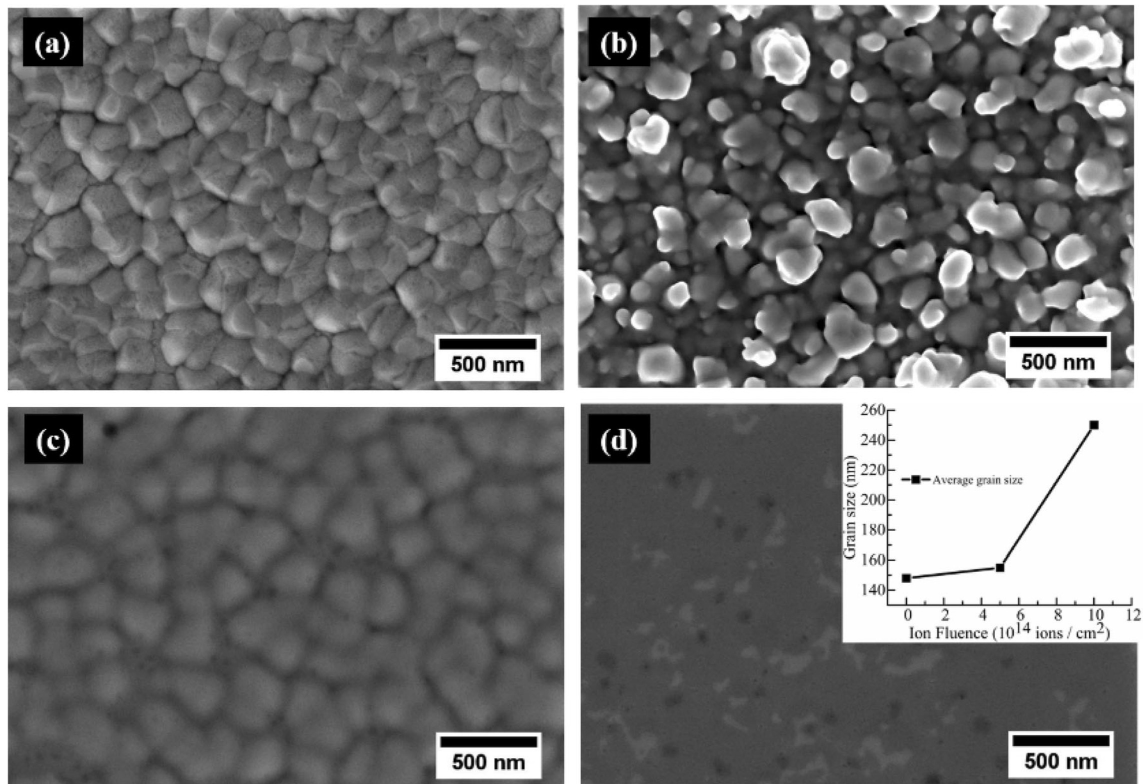

Fig. 1 SEM images of Ge ion-implanted $CoSb_3$: **a** GCS1, **b** GCS2, **c** GCS3 and **d** GCS4. Inset in **d** shows the calculated average grain size of GCS1, GCS2 and GCS3. The grain size increases with the increase in ion fluences

accelerating ion penetrates a solid, it loses its energy through nuclear as well as electronic energy loss. At low energy ion implantation, the nuclear energy process dominates and the target atom receives sufficient energy to produce a collision cascade leading to the formation of vacancies, interstitials etc. This forms the defect clusters, dislocation clusters and even extended defects as the implantation progresses. The production of these cascades leads to the promotion of diffusion which can lead to a variety of diffusion-based phase transformations including grain growth. The growth of grains starts from the crystalline-amorphous interface towards the surface and the rate of growth is proportional to the production of the rate of point defects. Mohanty et al. [33] studied the grain growth behaviour in tin oxide thin films by bombarding them with 250 keV Ar ion and proposed that the ion-induced defects enhance the diffusion of atoms and local annealing effects leads to the grain growth process. In another study, Karpe et al. [34] reported the irradiation-induced grain growth and associated it with the diffusion during the atomic collision cascade. For the sample at the highest ion fluence, i.e., at 5×10^{15} ions/cm^2, it is difficult to identify the grain growth at the same magnification level as that of the other three samples. The change in average grain size with fluence is shown in Fig. 1 [inset of (d)].

The topological views from AFM for the films of GCS1, GCS2, GCS3 and GCS4 are shown in Fig. 1a–d (scale area 1×1 μm^2). The surface roughness of GCS1 is 4.5 nm which increases considerably after the first ion fluence. The increase in roughness appears to be due to the sputtering caused during the ion implantation. The roughness of the film decreases and reaches $\sim$ 1.39 nm for the sample GCS4 (Fig. 2).

3.2 Structural properties

3.2.1 X-ray diffraction

The structure and phase of PLD deposited and Ge ion-implanted thin films were determined by GIXRD. Figure 3 shows the GIXRD patterns of GCS1, GCS2, GCS3 and GCS4. The indexing of the samples was done using the $CoSb_3$ (JCPDS No.-01-089-4039). The PLD grown films contain primarily the $CoSb_3$ phase

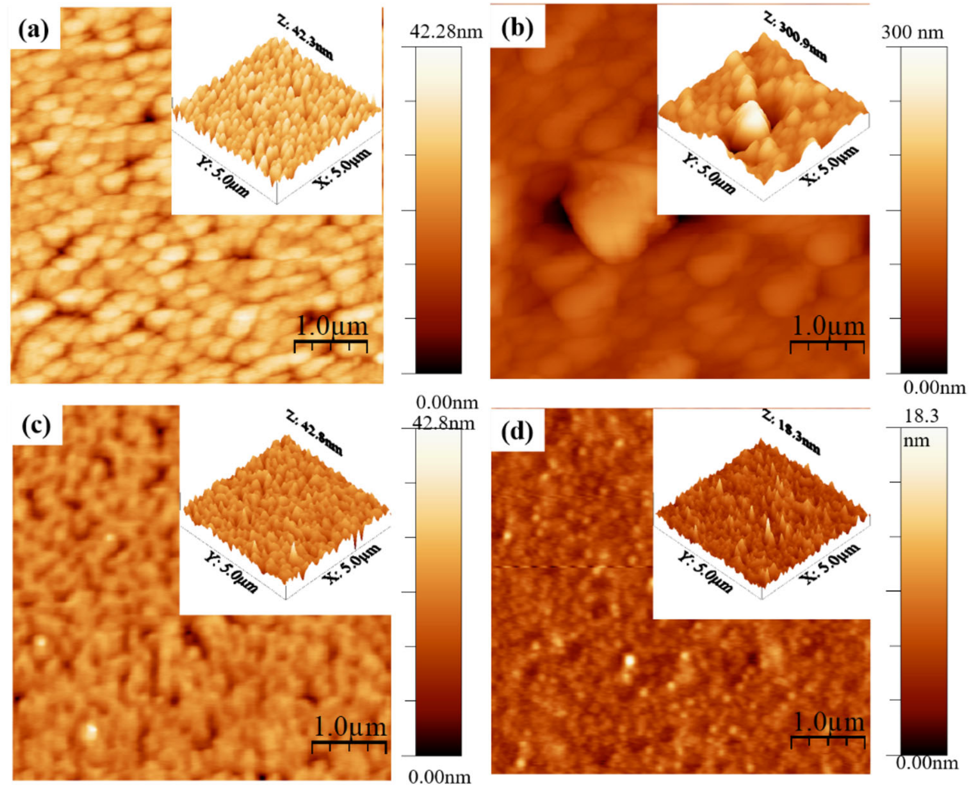

Fig. 2 AFM images of Ge ion-implanted samples: **a** GCS1, **b** GCS2, **c** GCS3 and **d** GCS4. Insets show the 3D images of the samples

and very small traces of the $CoSb_2$ phase. After Ge ion implantations, apart from the phase of $CoSb_3$, other phases such as $CoSb_2$ and oxides of Sb evolve (indicated by different symbols). The peaks intensity decreases considerably with the ion implantation, specifically, the intensities of main peaks related to reflections (013) and (123) of $CoSb_3$. This is possibly due to Ge occupying the voids in the $CoSb_3$ structure. A similar observation was reported by Nolas et al. [25] as they attempted to make Ge substituted La filled $IrSb_3$ compound. The authors reported that the decrease in intensity of the X-ray reflections is due to the filling of La atoms in the $IrSb_3$ voids. Takizawa [35] attempted to form the Ge filled $CoSb_3$ compound by varying the preparing pressure from 30 MPa to 5 GPa and reported that the decrease in reflection intensity of $Ge_xCo_4Sb_{12}$ is because of the incorporation of Ge atoms in the body-centred vacant sites of $CoSb_3$ host lattice. Hence, all these studies provide evidence to conclude that the Ge occupies the place in a void rather than taking the Sb position. The lattice parameter calculated for GCS1 is 0.915 nm, which matches well with the reported results [4]. Nevertheless, slight changes were observed in the lattice parameter after Ge ion implantation in the $CoSb_3$ host lattice. Crystallite size and lattice strain have been calculated from the most intense (013) Bragg peak, using Scherrer's formula [36]. The crystallite sizes of GCS1, GCS2 and GCS3 are 16, 19 and 13 nm, respectively. The lattice strains of GCS1, GCS2 and GCS3 are found to be 0.008, 0.007 and 0.10,

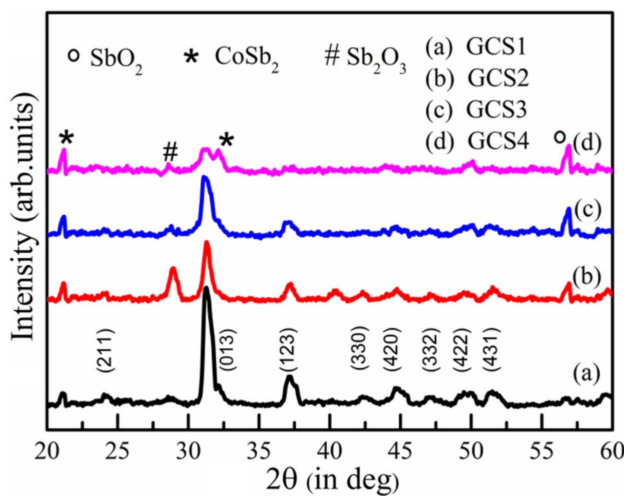

Fig. 3 GIXRD patterns of Ge ion-implanted thin films, GCS1, GCS2, GCS3 and GCS4. Only peaks corresponding to the $CoSb_3$ phase are marked with corresponding indices. SbO_2 phase is marked with o, $CoSb_2$ with * and Sb_2O_3 with #

respectively. Generally, it is considered that the grains are composed of several crystallites. Hence, in the present study, in the case of GCS1, its grain size is 148 nm which is composed of many crystallites of size 16 nm. Due to local disorder, the crystallite size and lattice strain of GCS4 could not be calculated.

3.2.2 *Raman spectroscopy*

The room temperature Raman scattering spectra recorded for GCS1, GCS2, GCS3 and GCS4 are presented in Fig. 4a. The resulting Raman peaks are fitted with the Lorentzian line shapes for GCS1 as shown in Fig. 4b. Out of the 19 optical modes ($6F_u + 4F_g + 2A_u + 2A_g + 3E_u + 2E_g$) that are expected to be present in unfilled skutterudite, nine of these Raman active modes ($F_u + 4F_g + 2E_g + 2A_g$) are assigned as the vibrations produced due to rattler atoms present in the voids and Sb atoms comprising the Sb_4 square planar ring. These assignments are based on theoretical studies. In this study, 7 out of 9 Raman active modes are observed. The atomic vibrations (v) of the seven Raman active modes and line width (Δv) of the Lorentzian fits of all the samples are displayed in Table 1. The modes are compared with the reported Ge filled $CoSb_3$ [27] and unfilled $CoSb_3$ theory [37]. The phonon frequencies in the present study match well with those reported for unfilled $CoSb_3$ confirming the formation of the $CoSb_3$ phase. The Raman active modes are the result of the vibration due to Sb–Sb bonds and are independent of Co atoms. These Raman scatterings help to elucidate the guest-host interactions in these particular skutterudites. As shown in Fig. 4a, the Raman spectra of the Ge implanted skutterudite films (GCS2, GCS3 and GCS4) are very similar to that of the pristine $CoSb_3$ (GCS1). The observed mode of frequencies for the implanted samples differs from the undoped skutterudite by 1–2 cm^{-1}. This suggests that the Ge ions are possibly situated in an off-centre position. From the fitting, one can observe the broadening of the peaks 121, 147, 158 and 179 cm^{-1}. The enhancement of these phonon line widths might be due to the phonon-phonon interaction. This broadening might also be triggered due to the random placement of Ge ion into the $CoSb_3$ structure by the implantation process. Further, during implantation, if some of the Ge ions occupied the voids, they may rattle inside them giving rise to the fluctuating bonding of the Sb bonds that forms the boundary of the voids. This might also lead to the slight broadening of the phonon linewidth of the Sb rings. When the atom rattles inside the void, it creates a disorder that affects the bonding of the Sb atoms that forms the void. This causes the broadening of the vibrational energies of the Raman active Sb vibrational modes. The Ge atoms while rattling inside the voids interact with lattice phonons. This is in corroboration with the low thermal conductivity of the $CoSb_3$ skutterudites. FT-IR is often considered complementary to Raman spectroscopy. It gives information based on the chemical composition and physical state of the sample and is recorded between 400 and 4000 cm^{-1}. Kumar et al.

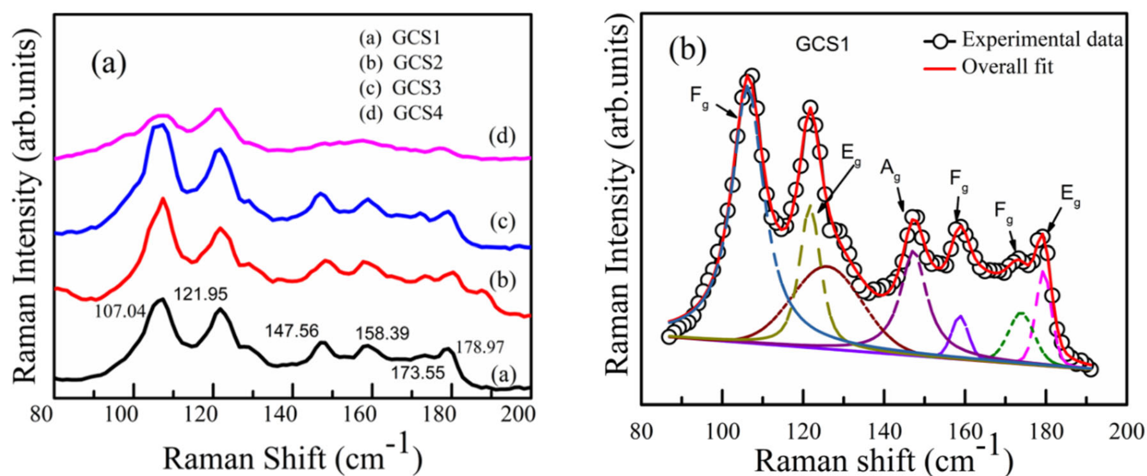

Fig. 4 **a** Raman spectra of Ge ion-implanted thin films of GCS1, GCS2, GCS3 and GCS4. **b** Fitted Raman peaks with Lorentzian line shapes for GCS1

Table 1 Peak positions, FWHM (in cm^{-1}) and mode assignments of the experimentally observed Raman active phonon modes of Ge ion-implanted thin films, GCS1, GCS2 and GCS3

GCS1 υ, $\Delta\upsilon$	GCS2 υ, $\Delta\upsilon$	GCS3 υ, $\Delta\upsilon$	$Ge_{0.05}CoSb_{12}$ υ, $\Delta\upsilon$	$CoSb_3$ theory υ
106, 10	107, 9	106, 9	110, 3	97 (F_g)
122, 6	122, 9	121, 7		
126, 20	130, 6	128, 17	136, 3	139 (E_g)
147, 7	149, 7	147, 9		150 (A_g)
159, 5	158, 8	159, 10	153, 4	157 (F_g)
174, 7	173, 7	172, 6	178, 5	178 (F_g)
179,4	180, 6	179, 7	180, 4	179 (A_g)

The peak positions are compared with $Ge_{0.005}$ $CoSb_{12}$ [27] and $CoSb_3$ theory [37]

[38] studied the FTIR analysis of In doped $CoSb_3$ (In = 0 to 0.0625). They reported that all the peaks in the regions 1600–1767 cm^{-1} correspond to metal-oxygen bonding whereas the peaks at 1387, 1384 and 1387 were assigned to Co-Sb bonding. Further, the peaks at 739, 738, 740 and 741 cm^{-1} were attributed to the Co complex and confirm the In filling in the void site of $CoSb_3$. FT-IR spectrum below 400 cm^{-1} is expected to provide more information about the phonon modes of vibration in the $CoSb_3$ samples. Raman scattering helps to elucidate the guest-host interaction in the skutterudites and the Raman active modes correspond to the vibrations of the Sb atoms. Raman spectroscopy results confirm the formation of the $CoSb_3$ phase as well as gives us information regarding the bonding between the constituent atoms and the position of Ge in the host lattice. This has been also discussed by Masarrat et al. [23] along with X-ray absorption spectroscopy data in the case of Fe ion-implanted $CoSb_3$.

3.3 Electrical resistivity and conduction mechanism

To understand the nature of electrical transport in Ge ion-implanted $CoSb_3$ thin films, the temperature-dependent resistivity was measured. Figure 5a shows the resistivity of samples GCS1, GCS2, GCS3 and GCS4 measured from 80 to 400 K. It is apparent that the resistivity decreases with temperature for all the samples depicting typical semiconducting behaviour. Moreover, the resistivity decreases considerably after the Ge ion implantation as compared to the pristine $CoSb_3$, i.e., GCS1. However, the decreasing rate of resistivity of ion-implanted samples is lower than the pristine $CoSb_3$. A similar feature was observed previously in Ge doped $CoSb_3$ [17, 15]. This change is mainly attributed to the increase in carrier concentration after Ge ion implantation. To verify this, room temperature Hall measurement was carried out on pristine as well as ion-implanted samples. The room temperature dependence of carrier concentration, mobility and the Hall coefficient is shown in Fig. 5b. All the samples are of n-type, which is in good agreement with the negative thermopower obtained in this work (discussed later). The carrier concentration of GCS1 is of the order of 10^{20} and increases to an order of magnitude after the ion implantation. The mobility, as well as the Hall coefficient, decreases with the increase in ion fluence. The defects and dislocations created during ion implantation result in a decrease in mobility [23]. The drastic decrease in resistivity after ion implantation is because of the considerable increase in charge carrier concentration with increasing ion fluence. It should be noted that the resistivity of GCS4 is higher than the other two ion-implanted samples. At the highest ion fluence, the distortion created by implantation might lead to a decrease in mobility and hence result in the increased electrical resistivity at the highest ion fluence, i.e., GCS4.

For the measured temperature range, the magnitude of bandgap can be calculated from the Arrhenius plot which is as given,

$$\rho(T) = \rho_0 \exp\left[\left(\frac{E_g}{2k_B T}\right)\right], \tag{1}$$

where ρ_0 is the residual resistivity, k_B is Boltzmann constant, T is the absolute temperature and E_g is the bandgap. The fitting of the straight line of ln ρ vs. $1/T$ gives the bandgap of 0.1 eV for GCS1 which is close to the value of $CoSb_3$ reported [4]. However, the bandgap calculation from the Arrhenius plot does not give very accurate values for narrow bandgap semiconductors. Hence, these calculated values just provide an idea of the relative variation of the bandgap of pristine $CoSb_3$ (GCS1) with that of the implanted samples (GCS2, GCS3 and GCS4). For the samples implanted with Ge, the bandgaps are 0.04, 0.02 and 0.04 eV, respectively. These values are much smaller than the bandgap of $CoSb_3$. The implantation of Ge ions modifies the band structure of $CoSb_3$ and

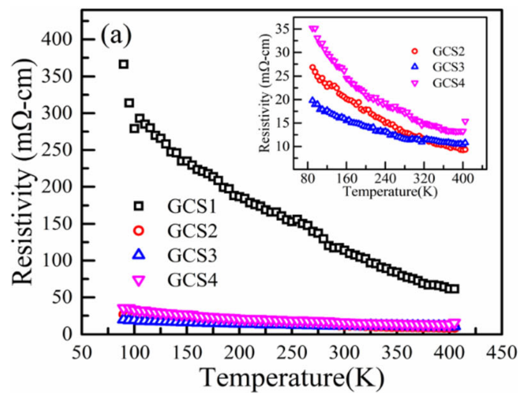

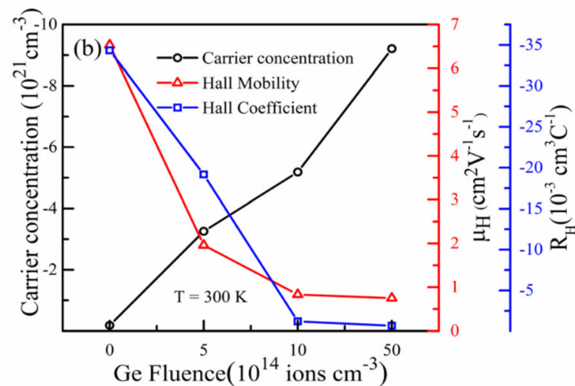

Fig. 5 **a** Temperature-dependent resistivity of Ge ion-implanted thin films, GCS1, GCS2, GCS3 and GCS4. All the films show semiconducting characteristics. Inset is the resistivity of GCS2, GCS3 and GCS4 and **b** Carrier concentration, Hall mobility and Hall coefficient as a function of Ge ion fluences

led to a change in bandgap values. The Ge ion introduces the donor levels in the bandgap of $CoSb_3$, which gets easily activated and hence leads to an increase in charge carrier concentration. It is evident from the Hall coefficient and hence decreases the resistivity. A similar introduction of donor levels in the bandgap was observed in the literature [18] due to In, and Yb dopants.

To understand the conduction mechanism of Ge ion-implanted thin films (GCS1, GCS2, GCS3 and GCS4), the temperature range is divided into two regimes: (i) low temperature (100 to 200 K), and (ii) high temperature (200 to 400 K). In 1968, Mott proposed that at low temperature, the states whose energies are within the narrow band near the Fermi level, follow the hopping conduction [39]. Thus, because of the narrow bandwidth, the constituent states can be considered as far from each other such that their spatial distribution is independent. Hence, the system that follows the VRH model assumes that the energy is independent of the density of states at the Fermi level. At low-temperature, Mott's variable range hopping (VRH) model based on localised electrons fits well for the low bandgap semiconductor and has a characteristic temperature dependence as

$$\rho = \rho_0 \exp\left[\left(\frac{T_M}{T}\right)^{1/4}\right], \tag{2}$$

where

$$T_M = \frac{C\alpha^3}{K_B N_F}, \tag{3}$$

where C is 18.1, α is the inverse of decay length, N_F is the density of localised states.

Figure 6a shows the plot of ln ρ vs. $1/T^{1/4}$ for the temperature range 80 to 200 K and fitted using Mott's VRH model for GCS1, GCS2, GCS3 and GCS4. The red solid line is shown in is the best fit of Eq. (2) of the experimental data. Previous studies have also reported that the electrical resistivity follows the VRH mechanism for $CoSb_3$ [40, 41]. Daniel et al. [40] studied the TE properties of Co–Sb thin films by varying the Sb concentration and identified the VRH as a dominant conduction mechanism at low temperatures. In another study, Bhaskar et al. [42] proposed that the electrical transport is dominated by Mott's theory of VRH in the temperature range of $300 \leq T \leq 425$ K for the $CoSb_{3(1+\delta)}$ system with $\delta = 0.00$, 0.01 and 0.02. Gharleghi et al. [43] also reported that for the temperature range 300 K $\leq T \leq$ 425 K, both resistivity and thermopower follow the VRH process for the $CoSb_3$ system which assumes the energy independence of density of states at the Fermi level. From fitting, T_M is calculated from the slope and listed in Table 2. T_M is found to be decreased as the Ge ion fluence increases. From Eq. 3, it is evident that T_M is inversely proportional to N_F, hence the density of states increases with Ge ion fluence. Further, the Mott hopping energy E_M can be evaluated by the following relation

$$E_M = \frac{1}{4} k_B T \left(\frac{T_M}{T}\right)^{\frac{1}{4}} \tag{4}$$

It can be seen that the activation energy monotonically decreases as $T^{3/4}$ with a decrease in temperature. For the same reason resistivity obeying Mott's law is often referred to as resistivity with decreasing

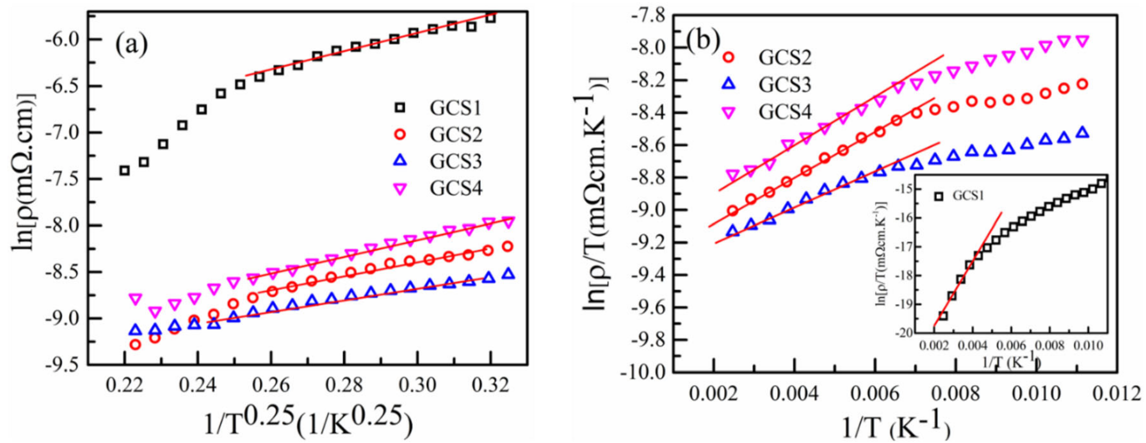

Fig. 6 **a** The plot of ln ρ vs. $1/T^{1/4}$ fitted using Mott's VRH model for GCS1, GCS2, GCS3 and GCS4. **b** The plot of ln ρ/T vs. $1/T$ in the framework of small polaron hopping conduction model at $T > 200$ K for GCS2, GCS3 and GCS4. Inset shows the fitting for GCS1

activation energy. The fitting suggests that the VRH process dominates the conduction for the temperature range from 100 to 200 K.

Linear behaviour of ln ρ vs. $T^{-1/4}$ plot is not observed in the temperature above 200 K and hence the resistivity data cannot be explained by the VRH model. In the temperatures above 200 K, the small polaron hopping conduction (SPHC) model is followed as given by the relation,

$$\rho(T) = \frac{1}{ne\mu} = \frac{T}{C}\exp\left(\frac{E_{hop}}{k_B T}\right), \quad (5)$$

where n is the carrier concentration, e is the electrical charge of the carrier, μ is the carrier mobility, C is a constant, E_{hop} is the activation energy of polaron hopping, and k_B is the Boltzmann constant. By plotting ln (ρ/T) vs. $1/T$ for all the samples (Fig. 6b), it is observed that the temperature dependence of resistivity fits well with the SPHC model for the given range of temperature (200 to 400 K). Generally, it is considered that electron-phonon coupling occurs in the vicinity of Fermi energy for the narrow bandgap semiconductors. Figure 7a shows the schematic of the $CoSb_3$ structure with the small polaron model (shown in a red dashed square). A schematic picture of the SPHC mechanism is shown in Fig. 7b. Electronic interactions between the electron (or holes) and the atom near these electrons give rise to localised atomic distortion. These distortions move along with electrons in the crystal lattice, which is called a *small polaron* [9]. According to the Holstein model, small polaron conduction occurs mainly through a thermally activated hopping process at high temperatures [44]. The activation energy E_{hop} of small polaron hopping is calculated by performing a linear fit to the experimental data of ln (ρ/T) versus $1/T$ plot and the values of E_{hop} all the Ge ion-implanted samples are shown in given in Table 2. It can be seen that the activation energy is smaller than the bandgap of $CoSb_3$. This indicates that the electrical conductivity in this temperature range is mainly due to small polaron hopping conduction and the intrinsic conduction does not occur within the measured temperature range. Yang et al. [45] studied the TE properties of $CoSb_3$ nanocomposites with dispersed nanoparticles and proposed that the system follow

Table 2 Seebeck coefficient, resistivity, mobility, carrier concentration, Hall coefficient, energy bandgap, Mott's temperature and hopping energy and other energy parameters derived from SPHC model of Ge ion-implanted thin films, GCS1, GCS2, GCS3 and GCS4 at room temperature

Sample	GCS1	GCS2	GCS3	GCS4
S(μV/K) (400 K)	− 45	− 18	− 15	− 6
ρ (mΩ cm)	114	12	11	15
μ ($cm^2 Vs^{-1}$)	6.53	1.96	0.83	0.74
N ($10^{20} cm^{-3}$)	− 1.815	− 32.56	− 51.85	− 92.1
R_H (10^{-2})	− 3.43	− 1.91	− 0.12	− 0.67
E_g (eV)	0.11	0.04	0.02	0.02
T_m (K)	14,641	7744	1099	7448
E_{hop} (eV)	0.089	0.02	0.01	0.01
E_S (eV)	0.03	0.01	0.01	0.004
W_H (eV)	0.059	0.01	–	0.06
E_P (eV)	0.12	0.02	–	0.12

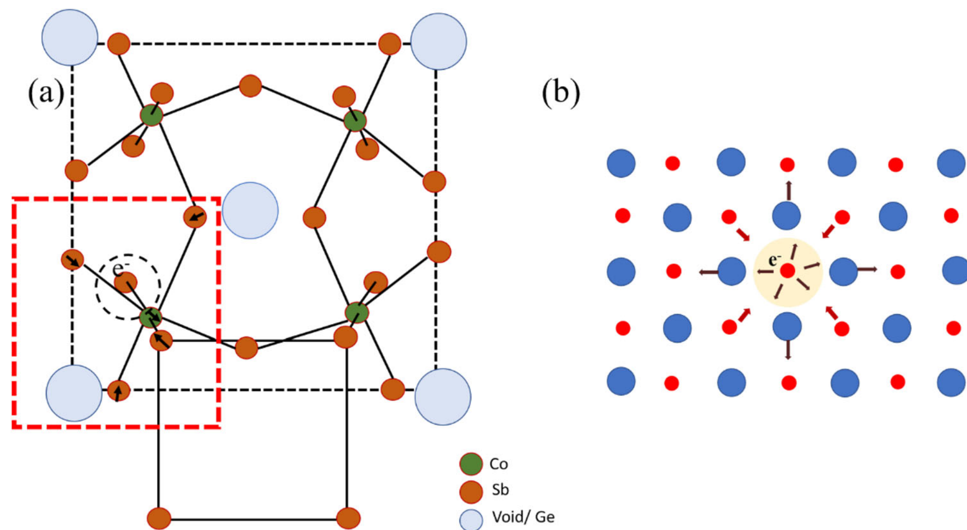

Fig. 7 **a** Schematic of $CoSb_3$ crystal structure. The conventional unit cell is shown with a black bold dashed line and Co, Sb and voids/Ge filled voids are indicated by green, brown and blue colours, respectively. One Sb_4 ring is also shown in the structure. The red bold dashed square shows one $CoSb_6$ octahedron showing the schematic of the small polaron model. Increasing temperature causes electronic interactions between e^- and the neighbouring atoms that give rise to local atomic distortions. These distortions move with e^- in the crystal lattice and are called small polarons. **b** the schematic of the polaron hopping model. The arrows represent the attractive and repulsive forces (Color figure online)

the Small polaron hopping model for the temperature above 250° while at low temperature the sample showed metallic behavior. Further, it is also observed that the E_{hop} decreases with the increase in Ge ion fluence. This suggests that the transport of polarons become easier with an increase in Ge concentration, which is consistent with the Hall measurement data (i.e., the Ge implanted samples have higher carrier concentration and low Hall mobility). Thus, the ion-implanted samples possess low electron mobility that may be due to the localized nature of charge carriers. Hence, the decrease in hopping energy for polaron transport facilitate charge transport and led to a decrease in electrical resistivity.

Figure 8 shows the temperature dependence of the Seebeck coefficient (S) for all the samples GCS1, GCS2, GCS3 and GCS4. The S values remain negative in the temperature range investigated for all the samples indicating the n-type behaviour. Electrons are the majority charge carriers as also confirmed by the Hall measurements. It is reported in the previous studies that Ge atoms occupying the void act as electron donors and that Ge substitutions on the Sb sites act as electron acceptors [17]. A similar case was observed for the Sn-filled $CoSb_3$ [17]. The magnitude of S increases with the increase in temperature for the full temperature range in all the samples. The low value of S is attributed to the presence of mixed phases of $CoSb_2$ and Sb_2O_3 along with the $CoSb_3$ phase. The value of the absolute Seebeck coefficient of multiphase films is usually lower than that of single-phase films [46]. The additional phases formed during deposition of films or implantation provides an additional path that short circuit the semiconducting phase. A previous study reported that the

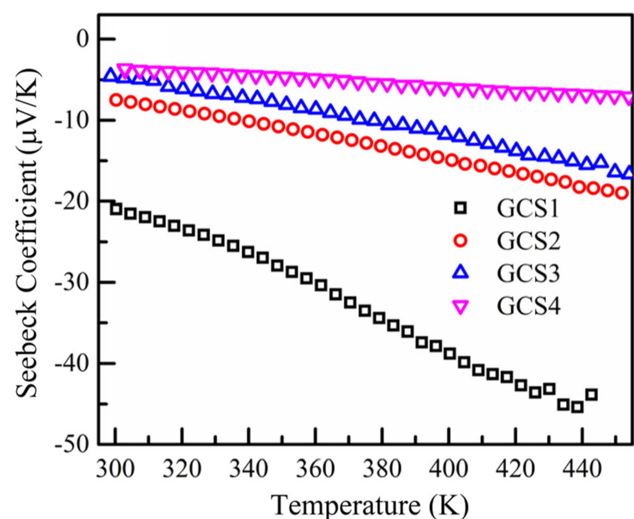

Fig. 8 Seebeck coefficient of Ge ion-implanted thin films, GCS1, GCS2, GCS3 and GCS4. The Seebeck coefficient is negative for all the films depicting n-type behaviour

S and charge carrier density decreases due to the presence of such impurity phases [40].

The absolute value of S decreases with the increase in ion fluence and depends on the carrier concentration n according to the relation,

$$S = \frac{8p^2K_B^2}{3eh^2}m^*T\left(\frac{p}{3n}\right)^{\frac{2}{3}}, \quad (6)$$

where S depends inversely on $n^{2/3}$. Hence, the S decreases as the carrier concentration increase, i.e., as ion fluence increases.

Mott's formula [47] for the thermopower can be used to extract the E_S, (activation energy for thermopower), which denotes the difference between the Fermi level and the polaronic band, i.e., the charge carrier generation energy in the polaronic picture.

$$S = -\frac{k}{e}\left(\frac{E_S}{k_BT} + A\right) \quad (7)$$

Here A is the constant of proportionality between heat transfer and kinetic energy of charge carriers. This activation energy derived from thermoelectricity can also be considered as the energy difference between identical lattice distortion with and without charge carriers [47].

The difference in activation energy derived from resistivity E_{hop} and that from thermopower E_S gives the energy required for polaron hopping, W_H, given as,

$$W_H = E_{hop} - E_S, \quad (8)$$

where $W_H > K_BT$ such that the thermally activated process dominates. One can further calculate the polaron formation energy from the relation, $E_P = 2W_H$. The above energies are listed in Table 2. Since $E_{hop} > E_S$it is the case for small polaron transportation.

The reduction of both R_H and ρ for the Ge ion-implanted thin films can be related to the defects and nanostructures created due to ion implantation. Usually, the largest Seebeck coefficient is recorded for the samples having a high ρ and large Hall coefficient [40]. A similar case is observed in the present study. The results from XRD, Raman and Seebeck coefficient suggest that in the Ge ion-implanted films, Ge ions can sit in the voids along with occupying the Sb sites. The positive attribute of the presence of Sb_2O_3 has low thermal conductivity ($\sim$ 0.4 Wm^{-1} K^{-1}) [48] as compared to that of $CoSb_3$ ($\sim$10 Wm^{-1} K^{-1}) [49]. Hence, the overall thermal conductivity may also decrease, which might enhance the overall efficiency of the system.

4 Conclusions

The morphological, structural and electrical properties of Ge ion-implanted $CoSb_3$ thin films are discussed. The grain growth is observed after the implantation which is attributed to the local annealing effect due to ion beam as well as to the creation of ion-induced defects. The Grazing incidence X-ray diffraction shows the presence of impurity phases of $CoSb_2$ and oxides of Sb along with the skutterudite phase. The Raman spectra of the implanted films (GCS2, GCS3 and GCS4) are very much similar to that of the pristine (GCS1), which suggest that the Ge ions might be present in an off-centre position. The decrease in the mobility and increase in the carrier concentration with the ion fluences lead to a decrease in electrical resistivity and these have positive attributes. The formation of nanostructures also accounts for reduced resistivity. Ge implantation leads to an increase in carrier concentration Further, the variable range hopping mechanism has been identified as the conduction mechanism for the low-temperature regime while small polaron hopping conduction fits well for the higher temperature region. The Hall measurements are in agreement with the thermopower results, which show that the films are of n-type.

Acknowledgements

Authors (KA and AM) are grateful to Indo-Taiwan bilateral project (Project No. GITA/DST/TWN/P-64/2015) under GITA-DST for this project funding. AM is thankful to Maulana Azad National Fellowship (MANF) for providing financial support including research fellowship.

Data availability

The data that support the findings of this study are available from the corresponding author upon reasonable request.

References

1. W.G. Zeier, New tricks for optimizing thermoelectric materials. Curr. Opin. Green Sustain. Chem. **4**, 23–28 (2017). https://doi.org/10.1016/j.cogsc.2017.02.003
2. G.J. Snyder, E.S. Toberer, Complex thermoelectric materials. Nat. Mater. **7**, 105–114 (2008). https://doi.org/10.1142/9789814317665_0016
3. G.A. Slack, V.G. Tsoukala, Some properties of semiconducting $IrSb_3$. J. Appl. Phys. **76**, 1665–1671 (1994). https://doi.org/10.1063/1.357750
4. G.S. Nolas, D.T. Morelli, T.M. Tritt, SKUTTERUDITES: a phonon-glass-electron crystal approach to advanced thermoelectric energy conversion applications. Annu. Rev. Mater. Sci. **29**, 89–116 (1999). https://doi.org/10.1146/annurev.matsci.29.1.89
5. S.K. Bux, J.-P. Fleurial, R.B. Kaner, Nanostructured materials for thermoelectric applications. Chem. Commun. **46**, 8311–8324 (2010). https://doi.org/10.1039/c0cc02627a
6. Z.-G. Chen, G. Han, L. Yang, L. Cheng, J. Zou, Nanostructured thermoelectric materials: current research and future challenge. Prog. Nat. Sci. Mater. Int. **22**, 535–549 (2012). https://doi.org/10.1016/j.pnsc.2012.11.011
7. K. Masood, P. Bin, Kumar, R.A. Singh, J. Singh, Odyssey of thermoelectric materials: foundation of the complex structure Odyssey of thermoelectric materials: foundation of the complex structure. J. Phys. Commun. **2**, 062001 (2018). https://doi.org/10.1088/2399-6528/aab64f
8. J.W. Sharp, E.C. Jones, R.K. Williams, P.M. Martin, B.C. Sales, Thermoelectric properties of CoSbs and related alloys. J. Appl. Phys. **78**, 1013–1018 (1995). https://doi.org/10.1063/1.360402
9. K. Matsubara, T. Sakakibara, Y. Notohara, H. Anno, H. Shimizu, T. Koyanagi, Electronic transport properties of the skutterudite CoSb and mixed alloys 3, in *Fifteenth International Conference on Thermoelectrics. Proceedings ICT '96*. (IEEE, Pasadena, 1996)
10. S. Yang, J. Si, Q. Su, H. Wu, Enhanced thermoelectric performance of SnSe doped with layered MoS_2/graphene. Mater. Lett. **193**, 146–149 (2017). https://doi.org/10.1016/j.matlet.2017.01.079
11. B.C. Sales, D. Mandrus, B.C. Chakoumakos, V. Keppens, J.R. Thompson, Filled skutterudite antimonides: electron crystals and phonon glasses. Phys. Rev. B **56**, 15081–15089 (1997). https://doi.org/10.1103/PhysRevB.56.15081
12. S. Katsuyama, Y. Kanayama, M. Ito, K. Majima, H. Nagai, Thermoelectric properties of $CoSb_3$ with dispersed $FeSb_2$ particles. J. Appl. Phys. **88**, 3484–3489 (2000). https://doi.org/10.1063/1.1288015
13. C. Chubilleau, B. Lenoir, C. Candolfi, P. Masschelein, A. Dauscher, E. Guilmeau, C. Godart, Thermoelectric properties of $In_{0.2}Co_4Sb_{12}$ skutterudites with embedded PbTe or ZnO nanoparticles. J. Alloys Compd. **589**, 513–523 (2014). https://doi.org/10.1016/j.jallcom.2013.11.204
14. A. Watcharapasorn, R.C. DeMattei, R.S. Feigelson, T. Caillat, A. Borshchevsky, G.J. Snyder, J.P. Fleurial, Preparation and thermoelectric properties of some phosphide skutterudite compounds. J. Appl. Phys. **86**, 6213–6217 (1999). https://doi.org/10.1063/1.371635
15. G.A.L. Lamberton Jr., S. Bhattacharya, R.T.L. Littleton IV., M.A. Kaeser, R.H. Tedstrom, T.M. Tritt, J. Yang, G.S. Nolas, High figure of merit in Eu-filled $CoSb_3$-based skutterudites. Appl. Phys. Lett. **80**, 598–600 (2002). https://doi.org/10.1063/1.1433911
16. V. Trivedi, M. Battabyal, P. Balasubramanian, G.M. Muralikrishna, P.K. Jain, R. Gopalan, Microstructure and doping effect on the enhancement of the thermoelectric properties of Ni doped Dy filled $CoSb_3$ skutterudites. Sustain. Energy Fuels. **2**, 2687–2697 (2018). https://doi.org/10.1039/c8se00395e
17. G.S. Nolas, J. Yang, H. Takizawa, Transport properties of germanium-filled $CoSb_3$. Appl. Phys. Lett. **84**, 5210–5212 (2004). https://doi.org/10.1063/1.1765205
18. S.R.S. Kumar, D. Cha, H.N. Alshareef, Lattice dynamics and substrate-dependent transport properties of (In, Yb)-doped $CoSb_3$ skutterudite thin films. J. Appl. Phys. **110**, 083710 (2011). https://doi.org/10.1063/1.3651382
19. E. Arushanov, K. Fess, W. Kaefer, C. Kloc, E. Bucher, Transport properties of lightly doped $CoSb_3$ single crystals. Phys. Rev. B **56**, 1911–1917 (1997). https://doi.org/10.1103/PhysRevB.56.1911
20. H. Anno, K. Matsubara, Y. Notohara, T. Sakakibara, H. Tashiro, Effects of doping on the transport properties of $CoSb_3$. J. Appl. Phys. **86**, 3780–3786 (1999). https://doi.org/10.1063/1.371287
21. M. Puyet, A. Dauscher, B. Lenoir, C. Bellouard, C. Stiewe, E. Müller, J. Hejtmanek, J. Tobola, Influence of Ni on the thermoelectric properties of the partially filled calcium skutterudites Cay. Phys. Rev. B **75**, 245110 (2007). https://doi.org/10.1103/PhysRevB.75.245110
22. M. Bala, A. Masarrat, A. Bhogra, R.C. Meena, Y. Lu, Y. Huang, C. Chen, C. Dong, S. Ojha, D.K. Avasthi, S. Annapoorni, K. Asokan, Structure and transport properties of nickel-implanted $CoSb_3$ skutterudite thin films synthesized via pulsed laser deposition. ACS Appl. Energy Mater. **1**, 5879–5886 (2018). https://doi.org/10.1021/acsaem.8b00646
23. A. Masarrat, A. Bhogra, R. Meena, M. Bala, R. Singh, V. Barwal, C.L. Dong, C.L. Chen, T. Som, A. Kumar, A. Niazi, K. Asokan, Effect of Fe ion implantation on the

thermoelectric properties and electronic structures of $CoSb_3$ thin films. RSC Adv. **9**, 36113–36122 (2019). https://doi.org/10.1039/c9ra06873b

24. M. Bala, A. Bhogra, S.A. Khan, T.S. Tripathi, S.K. Tripathi, D.K. Avasthi, M. Bala, A. Bhogra, S.A. Khan, T.S. Tripathi, S.K. Tripathi, Enhancement of thermoelectric power of PbTe thin films by Ag ion implantation. J. Appl. Phys. **121**, 215301–215309 (2017). https://doi.org/10.1063/1.4984050
25. G.S. Nolas, G.A. Slack, D.T. Morelli, T.M. Tritt, A.C. Ehrlich, The effect of rareearth filling on the lattice thermal conductivity of skutterudites. J. Appl. Phys. **79**, 4002–4008 (1996). https://doi.org/10.1063/1.361828
26. N. Shaheen, M.S. Javed, H.U. Shah, S. Hussain, M.A. Ahmad, R. Raza, M. Saleem, X. Zhou, Enhanced thermoelectric properties in Ge-doped and single-filled skutterudites prepared by unique melt-spinning method. Ceram. Int. **44**, 12610–12614 (2018). https://doi.org/10.1016/j.ceramint.2018.04.058
27. G.S. Nolas, C.A. Kendziora, H. Takizawa, Polarized Raman-scattering study of Ge and Sn-filled $CoSb_3$. J. Appl. Phys. **94**, 7440–7444 (2003). https://doi.org/10.1063/1.1628377
28. R.C. Mallik, E. Mueller, I.H. Kim, Thermoelectric properties of indium filled and germanium doped Co_4Sb_{12} skutterudites. J. Appl. Phys. **111**, 023708 (2012). https://doi.org/10.1063/1.3677982
29. J.F. Ziegler, M.D. Ziegler, J.P. Biersack, SRIM—the stopping and range of ions in matter (2010). Nucl. Instrum. Methods Phys. Res. Sect. B Beam Interact. Mater. Atoms. **268**, 1818–1823 (2010). https://doi.org/10.1016/J.NIMB.2010.02.091
30. M. Bala, R. Meena, S. Gupta, C. Pannu, T.S. Tripathi, S. Varma, S.K. Tripathi, K. Asokan, D.K. Avasthi, Formation of nanodots and enhancement of thermoelectric power induced by ion irradiation in PbTe: Ag composite thin films. Nucl. Inst. Methods Phys. Res. B. **379**, 36–41 (2016). https://doi.org/10.1016/j.nimb.2016.03.006
31. R.C. Mallik, R. Anbalagan, G. Rogl, E. Royanian, P. Heinrich, E. Bauer, P. Rogl, S. Suwas, Thermoelectric properties of $Fe_{0.2}Co_{3.8}Sb_{12-x}Te_x$ skutterudites. Acta Mater. **61**, 6698–6711 (2013). https://doi.org/10.1016/j.actamat.2013.07.032
32. D.K. Avasthi, G. Mehta, *Swift Heavy Ions for Material Engineering and Nanostructuring* (Springer, Berlin, 2011). https://doi.org/10.1007/978-94-007-1229-4
33. T. Mohanty, S. Dhounsi, P. Kumar, A. Tripathi, D. Kanjilal, 250 keV Ar^{2+} ion beam induced grain growth in tin oxide thin films. Surf. Coatings Technol. **203**, 2410–2414 (2009). https://doi.org/10.1016/j.surfcoat.2009.02.108
34. N. Karpe, J. Bottiger, N.G. Chechenin, J.P. Krog, Ion irradiation induced grain growth in nanocrystalline Fe and Fe (Zr). Mater. Sci. Eng. A **179**, 582–586 (1994). https://doi.org/10.1016/0921-5093(94)90271-2
35. H. Takizawa, K. Miura, M. Ito, T. Suzuki, T. Endo, Atom insertion into the $CoSb_3$ skutterudite host lattice under high pressure. J. Alloys Compd. **282**, 79–83 (1999). https://doi.org/10.1016/S0925-8388(98)00802-0
36. Z. Zheng, F. Li, J. Luo, G. Liang, H. Ma, X. Zhang, P. Fan, Thermoelectric properties and micro-structure characteristics of nano-sized $CoSb_3$ thin films prefabricating by co-sputtering. J. Alloys Compd. **732**, 958–962 (2018). https://doi.org/10.1016/j.jallcom.2017.10.207
37. J.L. Feldman, D.J. Singh, Lattice dynamics of skutterudites: first-principles and model calculations for $CoSb_3$. Phys. Rev. B **53**, 6273–6282 (1996). https://doi.org/10.1103/PhysRevB.53.6273
38. M. Uday Kumar, R. Swetha, L. Kumari, Synthesis, structure and optical properties of Indium filled $CoSb_3$ nanomaterials. J. Phys. Conf. Ser. **1495**, 012006 (2020). https://doi.org/10.1088/1742-6596/1495/1/012006
39. N.F. Mott, Conduction in glasses containing transition metal ions. J. Non. Cryst. Solids. **1**, 1 (1968). https://doi.org/10.1016/0022-3093(68)90002-1
40. M.V. Daniel, M. Lindorf, M. Albrecht, Thermoelectric properties of skutterudite $CoSb_3$ thin films. J. Appl. Phys. **120**, 125306–125301 (2016). https://doi.org/10.1063/1.4963111
41. J.S. Dyck, W. Chen, J. Yang, G.P. Meisner, C. Uher, Effect of Ni on the transport and magnetic properties of $Co_{1-x}Ni_xSb_3$. Phys. Rev. B **65**, 115204 (2002). https://doi.org/10.1103/PhysRevB.65.115204
42. A. Bhaskar, Y. Yang, Z. Yang, F. Lin, C. Liu, Fast fabrication and enhancement of thermoelectric power factor of p-type synthesis and evacuating-and-encapsulating sintering. Ceram. Int. **41**, 7989–7995 (2015). https://doi.org/10.1016/j.ceramint.2015.02.145
43. A. Gharleghi, C.J. Liu, Rapid fabrication and transport properties of n-type $Co_{4-x}Ni_xSb_{12}$ via modified polyol process synthesis combined with evacuated-and-encapsulated sintering. J. Alloys Compd. **592**, 277–282 (2014). https://doi.org/10.1016/j.jallcom.2014.01.020
44. T. Holstein, Studies of polaron motion part 2. The "Small" Polaron. Ann. Phys. (N. Y). **389**, 343–389 (1959). https://doi.org/10.1006/aphy.2000.6021
45. L. Yang, H.H. Hng, D. Li, Q.Y. Yan, J. Ma, T.J. Zhu, X.B. Zhao, H. Huang, Thermoelectric properties of p-type nanocomposites with dispersed nanoparticles. J. Appl. Phys. **106**, 013705 (2009). https://doi.org/10.1063/1.3157202
46. S.R.S. Kumar, A. Alyamani, J.W. Graff, T.M. Tritt, H.N. Alshareef, Pulsed laser deposition and thermoelectric properties of In- and Yb-doped $CoSb_3$ skutterudite thin film.

J. Mater. Res. **26**, 1836–1841 (2011). https://doi.org/10.1557/jmr.2011.198

47. Y. Natanzon, A. Azulay, Y. Amouyal, Evaluation of polaron transport in solids from first-principles. Isr. J. Chem. **60**, 1–20 (2020). https://doi.org/10.1002/ijch.201900101
48. K. Upadhyay, N. Goyal, S. Gautam, Solvothermal assisted synthesis of $CoSb_3$ phase evolution: morphology and electrical study for thermoelectric applications. Vacuum **163**, 142–147 (2019). https://doi.org/10.1016/j.vacuum.2019.02.003
49. D.W. Song, W.L. Liu, T. Zeng, T. Borca-Tasciuc, G. Chen, J.C. Caylor, T.D. Sands, Thermal conductivity of skutterudite thin films and superlattices. Appl. Phys. Lett. **77**, 3854 (2000). https://doi.org/10.1063/1.1329633

Publisher's Note Springer Nature remains neutral with regard to jurisdictional claims in published maps and institutional affiliations.